

X-Ray and high energy flares from late internal shocks of gamma-ray bursts

Y. W. Yu^{1,2} and Z. G. Dai¹

¹*Department of Astronomy, Nanjing University, Nanjing 210093, China;
yuyw, dzg@nju.edu.cn*

²*Institute of Astrophysics, Huazhong Normal University, Wuhan 430079, China*

ABSTRACT

We study afterglow flares of gamma-ray bursts (GRBs) in the framework of the late internal shock (LIS) model based on a careful description for the dynamics of a pair of shocks generated by a collision between two homogeneous shells. First, by confronting the model with some fundamental observational features of X-ray flares, we find some constraints on the properties of the pre-collision shells that are directly determined by the central engine of GRBs. Second, high energy emission associated with X-ray flares, which arises from synchrotron self-Compton (SSC) emission of LISs, is investigated in a wide parameter space. The predicted flux of high energy flares may reach as high as $\sim 10^{-8} \text{erg cm}^{-2} \text{s}^{-1}$, which is likely to be detectable with the Large Area Telescope (LAT) aboard *the Fermi Space Telescope* (formerly GLAST).

Subject headings: gamma rays: bursts — radiation mechanism: nonthermal

1. Introduction

Since the launch of the *Swift* satellite in 2004, the X-ray telescope (XRT) aboard has revealed several new features of early X-ray afterglow light curves of gamma-ray bursts (GRBs) (e.g., Mészáros 2006; Zhang 2007 for reviews): (i) the transition from prompt phase to afterglow phase usually exhibits steep decline of X-ray flux, which is generally interpreted as the high-latitude tail of prompt emission (i.e., curvature effect; Fenimore et al. 1996; Kumar & Panaitescu 2000;), (ii) a shallow decay usually follows the steep segment during the first hours, which could be caused by a spread of Lorentz factors in GRB ejecta (Rees & Mészáros 1998) or a continuous energy injection into GRB ejecta due to lasting activities of GRB central engines (e.g., Dai & Lu 1998a, 1998b; Zhang & Mészáros 2001a; Dai 2004; Fan & Xu 2006; Yu & Dai 2007), and (iii) bright X-ray flares superimposing on underlying

afterglow emission were observed from nearly a half of the *Swift* GRBs (Burrows et al. 2005; see Chincarini et al. 2007 and Falcone et al. 2007 for more recent statistic studies). These discoveries are of great importance for revealing the nature of GRB central engines, and especially, X-ray flares are widely accepted to be due to some delayed intermittent activities of the central engines.

In the sight of model, the delayed intermittent activities might be episodic accretion onto a central object due to a chopped accretion disk (Perna et al. 2006), or episodic accretion due to a modulation of the accretion flow by a magnetic barrier (Proga & Zhang 2006), or magnetic reconnection on a nascent differentially-rotating massive neutron star (Dai et al. 2006), etc. Many scenarios were designed in the past few years, but none of them is conclusive (see Zhang 2007 for a review). However, the key point is that, in almost all of these scenarios, internal dissipations in late-ejected materials are usually required to produce flare emission. The leading mechanism for internal dissipation is late internal shocks (LISs; Burrows et al. 2005; Fan & Wei 2005), which are generated by collisions among some shells ejected at different times with different Lorentz factors and energies. Hitherto, the properties of LIS-produced emission have been discussed for a few times (e.g., Fan & Wei 2005; Wu et al. 2005; Zhang et al. 2006; Zou et al. 2006; Fan et al. 2007; Galli & Guetta 2008). However, the properties of the pre-collision shells, which are directly determined by the late activities of the central engines, were not concerned in their works. In this paper, in contrast, we give a more detailed description for the dynamics of LISs including internal forward and reverse shocks, and then investigate the predicted X-ray flare luminosity and the shape of light curves within a wide model parameter space. By confronting the theoretical predictions with some observational features of X-ray flares, we can find some constraints on the model parameters.

Furthermore, it must be helpful to constrain the model more stringently by performing a simultaneous observation in the high-energy γ -ray bands for X-ray flares in the *Fermi* era. As suggested previously by Wang, Li, & Mészáros (2006), Fan & Piran (2006), and Galli & Guetta (2008), high energy flares are expected to arise from inverse Compton (IC) scattering of low-energy flare photons off some relativistic electrons. These electrons belong to either GRB ejecta (i.e. external inverse Compton, EIC) or flare ejecta self (i.e. synchrotron self-Compton, SSC). Based on the same consideration, we discuss the detectability of high energy flares in the *Fermi* era with the careful description for LIS dynamics along with the constraints from X-ray observations.

This paper is organized as follows: in section 2, we describe the dynamics of a pair of shocks arising from a collision between two homogeneous shells and the resulting synchrotron radiation of the shocked electrons. In section 3, the model is tested by some observational

features of X-ray flares. In section 4, we estimate the accompanying SSC high-energy emission and its detectability in the *Fermi* era. Finally, a summary is given in section 5.

2. The model

After the prompt phase of a GRB, the central engine might still be able to eject some separate shells with different Lorentz factors and energies due to its delayed intermittent activities. Collisions between these shells generate LISs, which give rise to the observed X-ray flares. For simplicity, the scope of the paper is restricted within one collision between two homogeneous shells.

2.1. Dynamics

We set the time zero point at the GRB trigger and measure time in the observer’s frame. At a time of $t_{\text{ej},A}$, the central engine ejects a shell denoted by A , which moves at a constant bulk Lorentz factor γ_A and carries an isotropic-equivalent kinetic energy luminosity $L_{\text{iso},A}$. The particle number density of the shell measured in its comoving frame (denoted by a prime hereafter) can be calculated by

$$n'_A = \frac{L_{\text{iso},A}}{4\pi R^2 \gamma_A^2 m_p c^3}, \quad (1)$$

where R is the radius of the shell. Some time (Δt_{ej}) later, another shell denoted by B with γ_B and $L_{\text{iso},B}$ is assumed to be ejected again. We require $\gamma_B > \gamma_A$ in order to let shell B catch up and collide with the prior shell A . Consequently, a collision between A and B takes place at the radius $R_{\text{col}} = \beta_A \beta_B c \Delta t_{\text{ej}} / (\beta_B - \beta_A)$ and the time $t_{\text{col}} = t_{\text{ej},A} + \beta_A \Delta t_{\text{ej}} / (\beta_B - \beta_A) - R_{\text{col}}/c$. For $(\gamma_A, \gamma_B) \gg 1$, they read

$$R_{\text{col}} \simeq \frac{2\gamma_A^2 c \Delta t_{\text{ej}}}{1 - (\gamma_A/\gamma_B)^2}, \quad (2)$$

$$t_{\text{col}} \simeq t_{\text{ej},A} + \frac{\Delta t_{\text{ej}}}{1 - (\gamma_A/\gamma_B)^2} \simeq t_{\text{onset}}. \quad (3)$$

The collision time t_{col} determines the observed onset time t_{onset} of a flare in physics. Strictly, t_{onset} should be mildly larger than t_{col} since the physical onset is usually buried by normal afterglow emission.

Due to the collision, a pair of shocks are generated, including a forward shock and a reverse shock that propagate into shells A and B , respectively. Separated by the two shocks and a contact discontinuity surface, the system is divided into four regions: (1) unshocked

shell A , (2) shocked shell A , (3) shocked shell B , and (4) unshocked shell B , bulk Lorentz factors of which are $\gamma_1 = \gamma_A$, $\gamma_2 = \gamma_3 \equiv \gamma$, and $\gamma_4 = \gamma_B$. Considering the motion of the shocked regions relative to unshocked regions 1 and 4, respectively, two relative Lorentz factors can be calculated by

$$\gamma_{21} = \frac{1}{2} \left(\frac{\gamma_1}{\gamma} + \frac{\gamma}{\gamma_1} \right), \quad \gamma_{34} = \frac{1}{2} \left(\frac{\gamma}{\gamma_4} + \frac{\gamma_4}{\gamma} \right). \quad (4)$$

Then, according to the jump conditions between the two sides of a shock (Blandford & McKee 1976), we can calculate the internal energy densities of the two shocked regions by $e'_2 = (\gamma_{21} - 1)(4\gamma_{21} + 3)n'_1 m_p c^2$ and $e'_3 = (\gamma_{34} - 1)(4\gamma_{34} + 3)n'_4 m_p c^2$, where $n'_1 = n'_A$ and $n'_4 = n'_B$. The mechanical equilibrium between the two shocked regions requires $e'_2 = e'_3$, which yields

$$\frac{(\gamma_{21} - 1)(4\gamma_{21} + 3)}{(\gamma_{34} - 1)(4\gamma_{34} + 3)} = \frac{n'_4}{n'_1} = \left(\frac{L_4}{L_1} \right) \left(\frac{\gamma_1}{\gamma_4} \right)^2 \equiv f. \quad (5)$$

For four given parameters, L_1 , L_4 , γ_1 , and γ_4 , that describe the basic properties of the pre-collision shells, we can obtain the value of γ by solving equations (4) and (5). In particular, for four limits shown in the $(\gamma_4/\gamma_1, L_4/L_1)$ parameter space (see Figure 1), these equations can be solved analytically. For $\gamma_4 \gg \gamma_1$, we have (i) if $L_4/L_1 \gg (1/7)(\gamma_4/\gamma_1)^4$,

$$\gamma_{21} = \frac{\gamma_4}{2\gamma_1} \gg 1 \quad \& \quad \gamma_{34} - 1 \approx \frac{\gamma_4^2}{7f\gamma_1^2} = \xi \ll 1; \quad \gamma = \gamma_4(1 - \sqrt{2\xi}), \quad (6)$$

which means the forward shock is relativistic and the reverse shock is Newtonian (RFS & NRS); (ii) if $16 \ll L_4/L_1 \ll (1/16)(\gamma_4/\gamma_1)^4$,

$$\gamma_{21} = \frac{f^{1/4}\gamma_4^{1/2}}{2\gamma_1^{1/2}} \gg 1 \quad \& \quad \gamma_{34} = \frac{\gamma_4^{1/2}}{2f^{1/4}\gamma_1^{1/2}} \gg 1; \quad \gamma = f^{1/4}\gamma_1^{1/2}\gamma_4^{1/2}, \quad (7)$$

which means both the forward and reverse shocks are relativistic (RFS & RRS); (iii) if $L_4/L_1 \ll 7$,

$$\gamma_{21} - 1 \approx \frac{f\gamma_4^2}{7\gamma_1^2} = \xi \ll 1 \quad \& \quad \gamma_{34} = \frac{\gamma_4}{2\gamma_1} \gg 1; \quad \gamma = \gamma_1(1 + \sqrt{2\xi}), \quad (8)$$

which means the forward shock is Newtonian whereas the reverse shock is relativistic (NFS & RRS). Finally, (iv) for $\gamma_4 \approx \gamma_1$, both the forward and reverse shocks are Newtonian (NFS & NRS). Since γ_1 , γ_4 , and the ratio f are unchanged with the moving of the shells, the values of γ as well as γ_{21} and γ_{34} can keep constant before the shocks cross the shells. In principle, when one shock crosses the corresponding shell, the other shock should be decelerated in the rest frame of its upstream material. However, if the energy carried by

the remaining unshocked material is much less than the energy of the total shocked material at that time, γ would be not changed significantly. So, we can treat with γ as a constant always approximately if we assume the crossing times of the two shocks to be equal more or less. After both shocks vanish, the merged shell no longer interacts with any other materials until it is caught up with by the third late-ejected shell.

The above analysis on kinematics and dynamics yields the evolution of the radius of the system after the collision,

$$R(t) = R_{\text{col}} + 2\gamma^2 c(t - t_{\text{col}}) \equiv R_{\text{col}} + 2\gamma^2 cT, \quad (9)$$

where we redefine the time T by resetting the time zero point from the GRB trigger to the flare onset time. We can define an initial expansion time from equation (9),

$$T_{\text{exp}} = \frac{R_{\text{col}}}{2\gamma^2 c} = \frac{\Delta t_{\text{ej}}}{1 - (\gamma_1/\gamma_4)^2} \left(\frac{\gamma_1}{\gamma} \right)^2, \quad (10)$$

and find that the increase of the radius before T_{exp} can be ignored (i.e. $R \simeq \text{constant}$) but after T_{exp} the radius increases linearly with time (i.e. $R \propto T$). Moreover, as the propagation of the shocks, the total electron numbers can be calculated by $N_{e,2} = 8\pi R^2 n'_1 (\gamma_{21}\beta_{21}/\gamma\beta)\gamma^2 cT$ and $N_{e,3} = 8\pi R^2 n'_4 (\gamma_{34}\beta_{34}/\gamma\beta)\gamma^2 cT$ for the two shocked regions (Dai & Lu 2002), both of which are proportional to T before the shock crossing.

2.2. Synchrotron radiation

For the two shocked regions, fractions ϵ_B and ϵ_e of the internal energy are assumed to be carried by magnetic fields and hot electrons, respectively. Then, the strength of the magnetic fields reads $B'_i = (8\pi\epsilon_B e'_i)^{1/2}$, whose variation is determined by the evolution of e'_i . Denoting the comoving volume of a shocked region as V'_i , we adopt $e'_i \propto V'^{-1}_i \propto R^{-2}$ by ignoring a possible spreading of the hot shocked materials. In the presence of the shocks that might be able to suppress the spreading of the hot materials, the neglect of the spreading may be plausible. However, after the shock crossing time T_{crs} (we assume here the two shocks cross at a similar time), the spreading of the hot materials into the vacuum cannot be ignored and the hot materials should experience an adiabatic cooling. During this phase, we assume that the volume of the merged shell is determined by a simple power-law as $V'_i \propto R^s$, where s is a free parameter and its value is taken from 2 to 3. Then, the particle number densities would decrease as $n'_i \propto V'^{-1}_i \propto R^{-s}$ and the internal energy densities as $e'_i \propto V'^{-4/3}_i \propto R^{-4s/3}$ due to adiabatic cooling. Therefore, a multi-power temporal behavior for the magnetic field

strength can be found:

$$B'_i \propto \begin{cases} T^0, & T < T_{\text{exp}}; \\ T^{-2s/3}, & T > T_{\text{exp}}; \end{cases} \quad T_{\text{crs}} < T_{\text{exp}}, \quad (11)$$

$$B'_i \propto \begin{cases} T^0, & T < T_{\text{exp}}; \\ T^{-1}, & T_{\text{exp}} < T < T_{\text{crs}}; \\ T^{-2s/3}, & T > T_{\text{crs}}; \end{cases} \quad T_{\text{crs}} > T_{\text{exp}}. \quad (12)$$

As usual, we assume that electrons are accelerated by the shocks to distribute as $dn'_{e,i}/d\gamma'_{e,i} \propto \gamma'^{-p}_{e,i}$ for $\gamma'_{e,i} > \gamma'_{e,m,i}$, where the minimum Lorentz factor is defined as $\gamma'_{e,m,i} = \epsilon_e C_p (m_p/m_e) (\gamma_{\text{rel}} - 1)$ with $C_p \equiv (p-2)/(p-1)$ and $\gamma_{\text{rel}} = \gamma_{21}$ or γ_{34} . Additionally, the cooling Lorentz factor, $\gamma'_{e,c,i} = 6\pi m_e c / [(1 + Y_i) \sigma_T B'^2_i \gamma T]$, also needs to be introduced, above which the electrons lose most of their energies. The Compton parameter Y_i defined as the ratio of the IC to synchrotron luminosities can be estimated by $Y_i \approx [(4\eta_i \epsilon_e / \epsilon_B + 1)^{1/2} - 1]/2$ with $\eta_i = \min[1, (\gamma'_{e,c,i} / \gamma'_{e,m,i})^{2-p}]$ (Sari & Esin 2001). Then, by calculating two characteristic frequencies and a peak flux density,

$$\nu_{m,i} = \frac{q_e}{2\pi m_e c} B'_i \gamma'^2_{e,m,i} \gamma, \quad \nu_{c,i} = \frac{q_e}{2\pi m_e c} B'_i \gamma'^2_{e,c,i} \gamma, \quad F_{\nu,\text{max},i} = \frac{N_{e,i} m_e c^2 \sigma_T}{4\pi d_L^2} \frac{B'_i \gamma}{3q_e}, \quad (13)$$

where d_L is the luminosity distance of the source, a multi-power synchrotron spectrum contributed by a shock can be written as (Sari et al. 1998)

$$F_{\nu,i} = F_{\nu,\text{max},i} \times \begin{cases} \left(\frac{\nu}{\nu_l}\right)^{1/3}, & \nu < \nu_l; \\ \left(\frac{\nu}{\nu_l}\right)^{-(q-1)/2}, & \nu_l < \nu < \nu_h; \\ \left(\frac{\nu_h}{\nu_l}\right)^{-(q-1)/2} \left(\frac{\nu}{\nu_h}\right)^{-p/2}, & \nu_h < \nu, \end{cases} \quad (14)$$

where $\nu_l = \min(\nu_{m,i}, \nu_{c,i})$, $\nu_h = \max(\nu_{m,i}, \nu_{c,i})$, and $q = 2$ for $\nu_{c,i} < \nu_{m,i}$ and $q = p$ for $\nu_{c,i} > \nu_{m,i}$.

To obtain X-ray light curves further, the temporal dependence of the characteristic quantities also needs to be presented as follows:

(i) In the case of $T_{\text{crs}} < T_{\text{exp}}$,

$$\nu_{m,i} \propto \begin{cases} T^0, & T < T_{\text{exp}}; \\ T^{-2s/3}, & T > T_{\text{exp}}, \end{cases} \quad (15)$$

$$\nu_{c,i} \propto \begin{cases} T^{-2}, & T < T_{\text{exp}}; \\ T^{2s-2}, & T > T_{\text{exp}}, \end{cases} \quad (16)$$

$$F_{\nu, \max, i} \propto \begin{cases} T, & T < T_{\text{crs}}; \\ T^0, & T_{\text{crs}} < T < T_{\text{exp}}; \\ T^{-2s/3}, & T > T_{\text{exp}}; \end{cases} \quad (17)$$

(ii) In the case of $T_{\text{crs}} > T_{\text{exp}}$,

$$\nu_{m, i} \propto \begin{cases} T^0, & T < T_{\text{exp}}; \\ T^{-1}, & T_{\text{exp}} < T < T_{\text{crs}}; \\ T^{-2s/3}, & T > T_{\text{crs}}, \end{cases} \quad (18)$$

$$\nu_{c, i} \propto \begin{cases} T^{-2}, & T < T_{\text{exp}}; \\ T, & T_{\text{exp}} < T < T_{\text{crs}}; \\ T^{2s-2}, & T > T_{\text{crs}}, \end{cases} \quad (19)$$

$$F_{\nu, \max, i} \propto \begin{cases} T, & T < T_{\text{exp}}; \\ T^0, & T_{\text{exp}} < T < T_{\text{crs}}; \\ T^{-2s/3}, & T > T_{\text{crs}}. \end{cases} \quad (20)$$

From the above expressions, we can see that $\nu_{c, i}$ reaches its minimum value at T_{exp} , while $\nu_{m, i}$ starts to decrease at the same time. So, the relationships between $\nu_{c, i}$ and $\nu_{m, i}$ as well as the spectra and light curves can be found easily by fixing and comparing the values of $\nu_{c, i}$ and $\nu_{m, i}$ at T_{exp} .

3. X-ray flares

Observations have shown that X-ray flares may consist of one or a few pulses. We consider one pulse to be mainly produced by one collision between two shells. Here we do not try to fit X-ray observational data in detail, which requires a more elaborate model that takes the fine structure of pre-collision shells into account. Instead, we only test the model by some fundamental observational features of X-ray flares.

3.1. X-ray luminosity

Statistic studies found that the average flare fluence (in 0.2 – 10 keV band) is approximately a factor of ten less than the fluence of prompt emission as $\sim 10^{-7}$ erg cm $^{-2}$ (Falcone et al. 2007) and the flare peak times t_{peak} concentrate into the range from 100 to 1000 s (Chincarini et al. 2007). Moreover, according to $\delta t/t_{\text{peak}} \ll 1$, the temporal width of flares,

δt , can be estimated to be from a few to several ten seconds. By considering the spread of the distributions of these quantities, we suggest to take $\sim 10^{-9}$ erg s $^{-1}$ cm $^{-2}$ as the lower limit for the peak flux of X-ray flares. For a typical luminosity distance $d_L = 10^{28}$ cm for GRBs, we give $\sim 10^{48}$ erg s $^{-1}$ as the lower limit for X-ray flare luminosity.

In order to derive some constraints on the model from this luminosity lower limit, first we show two (γ_1, γ_4) parameter spaces in Figure 2 with certain values of L_1 and L_4 : $L_4/L_1 \gg 1$ for the left panel and $L_4/L_1 = 1$ for the right panel, which correspond to different dynamic cases. According to the variation of ν_m^* and ν_c^* ,¹ the parameter spaces can be roughly divided into four regions denoted by ‘a, b, c, d’, where different relationships among ν_m^* , ν_c^* , and $\nu_X (\equiv 2.4 \times 10^{17}$ Hz) are given as listed in Table 1. We then use some shaded contours to show the regions where model-predicted X-ray luminosity exceeds the observational lower limit. Obviously, region ‘a’ is restricted significantly by this luminosity constraint due to the slow cooling of electrons (as indicated by $\nu_m^* < \nu_X < \nu_c^*$) that leads to a low radiation efficiency. To be more specific, we can conclude further that (i) in order to produce sufficiently strong flare emission, it is required that $\gamma_4 > \text{few} \times \gamma_1$. This means that at least one of the forward and reverse shocks is mild-relativistic; and (ii) when $\gamma_4 \approx \text{few} \times \gamma_1^2$, we can obtain the highest theoretical X-ray luminosity, because this parameter region roughly locates the boundary between regions ‘c’ and ‘d’, where the relationship $\nu_c^* < \nu_X \sim \nu_m^*$ can be found, indicating a high X-ray radiation efficiency. Second, in order to uncover the dependence of the emission on parameters L_1 and L_4 , we also show two corresponding parameter spaces in Figure 3 with certain values of γ_1 and γ_4 . A minimum value of $\sim 10^{50} - 10^{51}$ erg s $^{-1}$ for L_4 can be found, but the constraint on L_1 is loose. This indicates that the resulting X-ray luminosity is mainly determined by the kinetic-energy luminosity of the lagged rapid shell rather than that of the leading slow shell.

Finally, in the above calculations for X-ray luminosity, we ignored possible synchrotron self-absorption of the X-ray photons, which is able to suppress the X-ray emission. The synchrotron self-absorption thickness at the X-ray band can be calculated by (Panaitescu & Kumar 2000)

$$\tau_{ssa, \nu_X} \simeq \frac{5q_e N_e}{4\pi R^2 B^l \gamma_{e,l}^{l/5}} \times \begin{cases} \left(\frac{\nu_X}{\nu_l}\right)^{-5/3}, & \nu_X < \nu_l; \\ \left(\frac{\nu_X}{\nu_l}\right)^{-(q+4)/2}, & \nu_l < \nu_X < \nu_h; \\ \left(\frac{\nu_h}{\nu_l}\right)^{-(q+4)/2} \left(\frac{\nu_X}{\nu_h}\right)^{-(p+5)/2}, & \nu_h < \nu_X, \end{cases} \quad (21)$$

¹The star superscription represents that the values are calculated at the time of T_{exp} . We obtain the values of ν_m^* and ν_c^* from the spectrum due to the shock that dominates the X-ray emission and thus the subscription i of the quantities is omitted in this section.

where $\nu_l = \min(\nu_m, \nu_c)$, $\nu_h = \max(\nu_m, \nu_c)$, $\gamma'_{e,l} = \min(\gamma'_{e,m}, \gamma'_{e,c})$, and $q = 2$ for $\nu_c < \nu_m$ and $q = p$ for $\nu_c > \nu_m$. By scanning the whole parameter spaces shown in Figures 2 and 3, we find that the values of τ_{ssa, ν_X} are always much lower than unity due to the large internal shock radius, which means the synchrotron self-absorption of the X-ray photons can be ignored safely.

3.2. Shape of X-ray light curves

We here test the model by considering the shape of the observed X-ray flare light curves, a basic feature of which is the rapid rise and fall. Following the frequency relationships given in Table 1, we can find three possible types of the theoretical X-ray light curves, as shown schematically by the black lines in Figure 4 for $T_{\text{crs}} \simeq T_{\text{exp}}$ where the time zero is set at the flare onset time. The light curves break at several characteristic times and the corresponding temporal indices ($\alpha = -d \log F_\nu / d \log T$) are listed in Table 1. All of the segments after T_{crs} are steepened significantly by the shock crossing effect. By confronting these theoretical light curves with the observed ones, on one hand, it is easy to understand the observed steep rise by resetting the time zero point of the log-log figure from the flare onset time to the GRB trigger. On the other hand, as discovered by Liang et al. (2006), the rapid decline of most X-ray flares seems to be consistent with the curvature effect that predicts a temporal index being equal to the simultaneous spectral index plus 2. As shown by the black lines in Figure 4, the intrinsic decline slope of the last segment is $\alpha = (sp + s)/3$ for all types of the theoretical light curves and the corresponding spectral index is $(p - 1)/2$ due to $\nu_m < \nu_X < \nu_c$. For $s = 3$ and $2 < p < 3$, the inequation

$$\frac{(sp + s)}{3} > \frac{(p - 1)}{2} + 2 \quad (22)$$

can be satisfied easily. This inequation indicates that, in any case in our model, the observed X-ray flux decay should be dominated by the curvature effect, as shown by the grey lines in Figure 4. In addition, although some relatively flat segments with $\alpha = (3 - s)/3$ or $(sp - 2s + 3)/3$ appear in types II and III light curves, we still cannot rule out any one of them absolutely, because these segments that could not be very far from the flare onset time may be steepened by the time zero effect dramatically.

4. High energy flares

Because a part of the synchrotron photons would be boosted to higher energy by their IC scattering off some relativistic electrons, high energy counterparts of X-ray flares are

expected naturally. In the following calculations, we restrict our attention within the LIS model and SSC scenario. Before a specific calculation for the SSC emission, we first estimate the flux sensitivity of the LAT aboard the *Fermi* by

$$F_{\text{thr}} = \frac{5E}{A_{\text{eff}}t} = 1.33 \times 10^{-9} \left(\frac{E}{\text{GeV}} \right) \left(\frac{t}{10^3 \text{s}} \right)^{-1} \text{ erg cm}^{-2} \text{ s}^{-1}, \quad (23)$$

following Zhang & Mészáros (2001b) who adopted the criterion that at least five photons are collected if the instrument is source dominated, where E is the photon energy and t is the integration time. The effective area A_{eff} of the instrument is taken as a constant of 6000 cm² and the dependence of the area on the photon energy is neglected. However, after a transition time of $\sim 2.4 \times 10^4$ s (Gou & Mészáros 2007; Yu et al. 2007), the sensitivity should start to scale as $t^{-1/2}$ due to a limitation by the background for a long-time observation.

Following Sari & Esin (2001), the SSC spectrum contributed by a shock can be obtained by shifting the seed synchrotron spectrum to higher energy range, i.e. estimating the two break frequencies and the peak flux density of the SSC spectrum respectively by

$$\nu_{m,i}^\dagger = 2\gamma_{e,m,i}'^2 \nu_{m,i}, \quad \nu_{c,i}^\dagger = 2\gamma_{e,c,i}'^2 \nu_{c,i}, \quad F_{\nu,\text{max},i}^\dagger = \frac{\sigma_T N_{e,i}}{4\pi R^2} F_{\nu,\text{max},i}. \quad (24)$$

This approximative treatment is finely valid when the effect of the Klein-Nishina suppression is unimportant. Considering the highest-energy electrons whose energy enter the Klein-Nishina regime, we refer to the third break in the SSC spectrum,

$$\nu_{\text{KN},i} = \frac{\gamma^2 m_e^2 c^4}{h^2 \max(\nu_{m,i}, \nu_{c,i})}, \quad (25)$$

above which the SSC spectrum follows $F_{\nu,i} \propto \nu^{-(p-1)}$ (Gupta & Zhang 2007; Fragile et al. 2004). Therefore, the approximative SSC spectrum can be summarized as follows (Gupta & Zhang 2007)

$$F_{\nu,i}^\dagger = F_{\nu,\text{max},i}^\dagger \times \begin{cases} \left(\frac{\nu}{\nu_l} \right)^{1/3}, & \nu < \nu_l; \\ \left(\frac{\nu}{\nu_l} \right)^{(q-1)/2}, & \nu_l < \nu < \nu_h; \\ \left(\frac{\nu_h}{\nu_l} \right)^{-(q-1)/2} \left(\frac{\nu}{\nu_h} \right)^{-p/2}, & \nu_h < \nu < \nu_{\text{KN},i}; \\ \left(\frac{\nu_h}{\nu_l} \right)^{-(q-1)/2} \left(\frac{\nu_{\text{KN},i}}{\nu_h} \right)^{-p/2} \left(\frac{\nu}{\nu_{\text{KN},i}} \right)^{-(p-1)}, & \nu_{\text{KN},i} < \nu, \end{cases} \quad (26)$$

where $\nu_l = \min(\nu_{m,i}^\dagger, \nu_{c,i}^\dagger)$, $\nu_h = \max(\nu_{m,i}^\dagger, \nu_{c,i}^\dagger)$, and $q = 2$ for $\nu_{c,i}^\dagger < \nu_{m,i}^\dagger$ and $q = p$ for $\nu_{c,i}^\dagger > \nu_{m,i}^\dagger$.

Using equation (26), we calculate the peak flux of GeV γ -ray flares as shown by the shaded contours in Figure 5. Comparing these GeV emission contours with the dashed

contours that correspond to the X-ray luminosity, a positive correlation between these two emission components can be found. For the GRBs at a typical distance of 10^{28} cm, the high energy counterparts of the relatively brighter X-ray flares could be detected by the LAT, whereas those associated with weaker X-ray flares leak. The LAT sensitivity here ($\text{few} \times 10^{-9} \text{ erg s}^{-1} \text{ cm}^{-2}$) is calculated for a typical flare onset time of several hundred seconds and represented by the dash-dotted line in the figure. Furthermore, according to the expression of $Y_i \approx [(4\eta_i\epsilon_e/\epsilon_B + 1)^{1/2} - 1]/2$, we know that the relative importance of the SSC and synchrotron emissions may be sensitive to the parameters ϵ_B and ϵ_e . Therefore, we show the GeV γ -ray flux at the time of T_{exp} varying in the (ϵ_e, ϵ_B) parameter space in Figure 6. It can be seen that the high energy flux is mainly sensitive to ϵ_e and equipartition values for ϵ_e are required. In addition, we would like to show some example spectra numerically in Figure 7 using a more elaborate code that was developed in Yu et al. (2007).

5. Summary and discussion

The LIS model is usually employed to explain the observed GRB afterglow X-ray flares. However, a careful description for LIS dynamics and some observational constraints on it still need to be investigated. Based on this consideration, we studied the properties of LIS-produced emission in the framework of a simplified paradigm, i.e. internal forward-reverse shocks generated by a collision between two homogeneous shells. With a lower limit for the observed X-ray luminosity, we found a mildly high ratio of the Lorentz factors of pre-collision shells, which leads to at least one mildly-relativistic internal shock. Our results also show that the brightest X-ray flares might imply a high variability of Lorentz factors as indicated by $\gamma_4 = \text{few} \times \gamma_1^2$. The luminosity of the X-ray flares is mainly determined by the kinetic energy luminosity of the delayed rapid shell rather than the leading slow shell. After an investigation of the characteristic frequencies in a wide parameter space, three types of theoretical X-ray light curves are found, all of which are ended by a very steep decay with $\alpha \sim p + 1$. This indicates that the flare emission during the decay phase is probably dominated by the curvature effect, which is consistent with the observational inference found by Liang et al. (2006).

We also investigated the peak flux of the GeV γ -ray counterparts in the SSC scenario. By comparing the GeV flux with the flux sensitivity of the *Fermi* LAT, we found that the high energy flares associated with relatively brighter X-ray flares could be detected by the LAT for a distance of 10^{28} cm to the source, where an equipartition value of ϵ_e is required. This possible detection will be very helpful to discriminate different origins of high energy flares and different models for X-ray flares. As mentioned above, two types of high energy

flares are predicted by the LIS model including the ones due to the SSC and EIC emission. In the SSC case, a good temporal correlation between the X-ray and high energy flares are expected, whereas a significant temporal extension appears for high energy flares in the EIC case (Fan et al. 2007). In addition, besides the LIS model, some authors suggested that X-ray flares may be produced by a delayed external shock and the corresponding high energy emission was also expected (Galli & Piro 2007). But for the delayed afterglow model it is difficult to explain the reoccurrence of X-ray flares in one GRB afterglow.

Acknowledgements

This work is supported by the National Natural Science Foundation of China (grants no. 10221001, 10640420144, and 10873009) and the National Basic Research Program of China (973 program) No. 2007CB815404. YWY is also supported by the Scientific Innovation Foundation of Huazhong Normal University, the Visiting PhD Candidate Foundation of Nanjing University and the National Natural Science Foundation of China (grant 10773004).

REFERENCES

- Blandford, R. D., & McKee, C. F. 1976, *Phys. Fluids*, 19, 1130
- Burrows, D. N., Romano, P., Falcone, A., Kobayashi, S., Zhang, B., Moretti, A., O’Brien, P. T., Goad, M. R. et al. 2005, *Science*, 309, 1833
- Chincarini, G., Moretti, A., Romano, P., Falcone, A.D., Morris, D., Racusin, J., Campana, S. et al. 2007, *ApJ*, 671, 1903
- Dai, Z. G. 2004, *ApJ*, 606, 1000
- Dai, Z. G., & Lu, T. 1998a, *A&A*, 333, L87
- Dai, Z. G., & Lu, T. 1998b, *Phys. Rev. Lett.*, 81, 4301
- Dai, Z. G., & Lu, T. 2002, *ApJ*, 565, L87
- Dai, Z. G., Wang, X. Y., Wu, X. F., & Zhang, B. 2006, *Science*, 311, 1127
- Falcone, A. D., Morris, D., Racusin, J., Chincarini, G., Moretti, A., Romano, P., Burrows, D. N., Pagani, C. et al. 2007 *ApJ*, 671, 1921
- Fan, Y. Z., Piran, T., Narayan, R., & Wei, D. M. 2008, *MNRAS*, 384, 1483

- Fan, Y. Z., & Piran, T. 2006, MNRAS, 370, L24
- Fan, Y. Z., & Wei, D. M. 2005, MNRAS, 364, L42
- Fan, Y. Z., & Xu D. 2006, MNRAS, 372, L19
- Fenimore, E. E., Madras, C. D., & Nayakshin, S. 1996, ApJ, 473, 998
- Fragile, P. C., Mathews, G. J., Poirier, J., & Totani, T. 2004, Astropart. Phys., 20, 591
- Kumar, P. & Panaitescu, A. 2000, ApJ, 541, L51
- Liang, E. W. et al., 2006, ApJ, 646, 351
- Galli, A., & Guetta, D. 2008, A&A, 480, 5
- Galli, A., & Piro, L. 2007, A&A, 475, 421
- Gou, L. J., & Mészáros, P. 2007, ApJ, 668, 392
- Gupta, N., & Zhang, B. 2007, MNRAS, 380, 78
- Mészáros, P. 2006, Rept.Prog.Phys., 69, 2259
- Panaitescu, A., & Kumar, P. 2000, ApJ, 543, 66
- Perna, R., Armitage, P. J., & Zhang, B. 2006, ApJ, 636, L29
- Proga, D., & Zhang, B. 2005, MNRAS, 370, L61
- Rees, M. J., & Mészáros, P., 1998, ApJ, 496, L1
- Sari, R., Piran, T., & Narayan, R. 1998, ApJ, 497, L17
- Sari, R., & Esin, A. A. 2001, ApJ, 548, 787
- Wang, X. Y., Li, Z., & Mészáros, P. 2006, ApJ, 641, L89
- Wu, X. F., Dai, Z. G., Huang, Y. F., Feng, L. L., & Lu T. 2005, arXiv: astro-ph/0512555
- Yu, Y. W., & Dai, Z. G. 2007, A&A, 470, 119
- Yu, Y. W., Liu, X. W., & Dai, Z. G. 2007, ApJ, 671, 637
- Zhang, B. 2007, ChJAA, 7, 1

Zhang, B., Fan, Y. Z., Dyks, J., Kobayashi, S., Mészáros, P., Burrows, D. N., Nousek, J. A., & Gehrels, N. 2006, 642, 354

Zhang, B., & Mészáros, P. 2001a, ApJ, 552, L35

Zhang, B., & Mészáros, P. 2001b, ApJ, 559, 110

Zou, Y. C., Dai, Z. G., & Xu, D. 2006, ApJ, 646, 1098

This preprint was prepared with the AAS L^AT_EX macros v5.2.

Table 1: Four possible relationships (a, b, c and d) between ν_m^* , ν_c^* , and ν_X and three types (I–III) of the corresponding X-ray flare light curves (characterized by the temporal indices).

Regimes	Types	Temporal Indices (α)
a: $\nu_m^* < \nu_X < \nu_c^*$	I	$-1, \frac{sp+3}{3}$
b: $\nu_m^* < \nu_c^* < \nu_X$	II	$-1, 0, \frac{sp-2s+3}{3}, \frac{sp+3}{3}$
c: $\nu_c^* < \nu_m^* < \nu_X$	II	$-1, 0, \frac{sp-2s+3}{3}, \frac{sp+3}{3}$
d: $\nu_c^* < \nu_X < \nu_m^*$	III	$-1, -\frac{5}{3}, 0, \frac{3-s}{3}, \frac{sp-2s+3}{3}, \frac{sp+3}{3}$

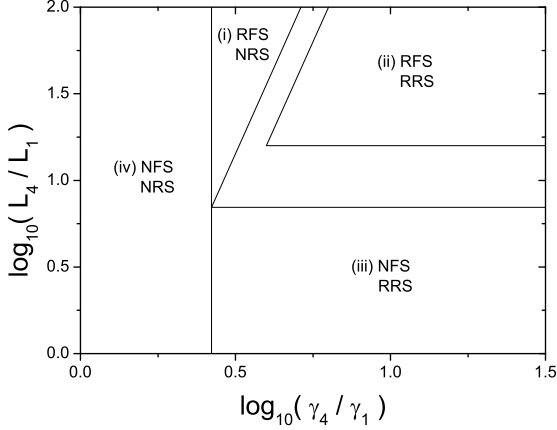


Fig. 1.— Regions in the $(\gamma_4/\gamma_1, L_4/L_1)$ parameter space where four limits of the LIS dynamics are given.

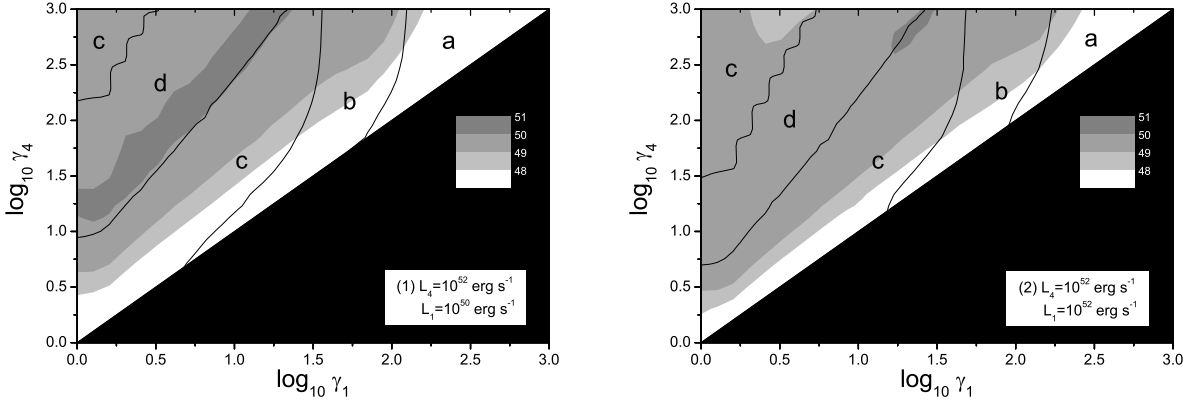


Fig. 2.— X-ray luminosity in the (γ_1, γ_4) parameter spaces. The regions where the model-predicted X-ray luminosity exceeds the observational lower limit ($\sim 10^{48}\text{erg s}^{-1}$) are presented by shaded contours, while the unshaded region is ruled out by this luminosity constraint. Separating by solid lines, the parameter spaces are divided into different regions denoted by “a, b, c, d”, where different relationships between ν_c^* , ν_m^* , and ν_X are given as listed in Table 1. The fixed values of the kinetic-energy luminosities of the shells satisfy $L_4/L_1 \gg 1$ for the left panel and $L_4/L_1 = 1$ for the right panel, and their corresponding dynamic cases can be found in Figure 1. The black region is forbidden due to $\gamma_4 < \gamma_1$. The other model parameters ϵ_B , ϵ_e , p , and Δt_{ej} are taken to be typical values of 0.03, 0.3, 2.5, and 100s, respectively.

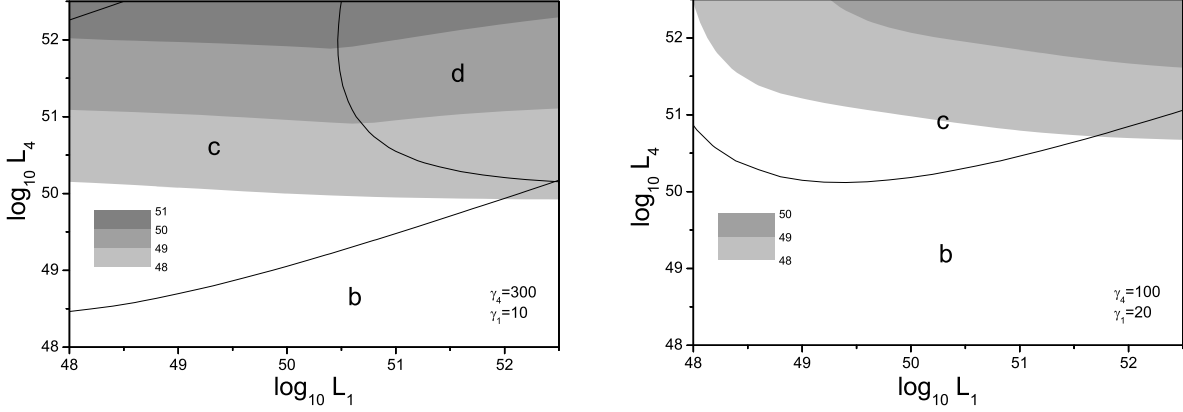


Fig. 3.— X-ray luminosity in the (L_1, L_4) parameter spaces. The left and right panels correspond to relatively higher and lower values of the ratio γ_4/γ_1 , respectively. The meanings of the regions and the other model parameters are the same as those in Figure 2.

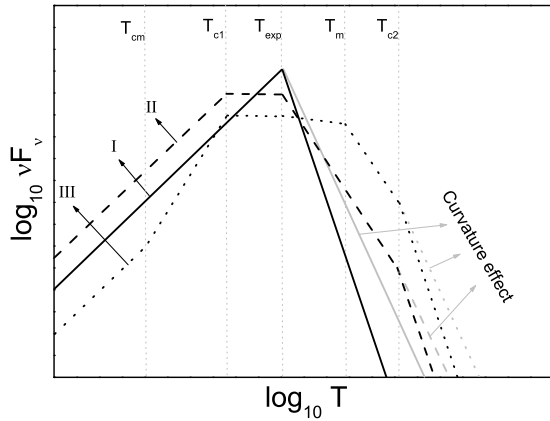


Fig. 4.— Schematic illustration of theoretical X-ray flare light curves for $T_{\text{crs}} = T_{\text{exp}}$ (black lines; the temporal indices of all segments are listed in Table 1). The curvature effect is exhibited by the grey lines. The vertical dotted lines represent the break times of the light curves, specifically, the time T_{cm} at which $\nu_c = \nu_m$, the time T_m (T_c) at which the break frequency ν_m (ν_c) passes through the X-ray band, the time T_{exp} from which the radius increases linearly.

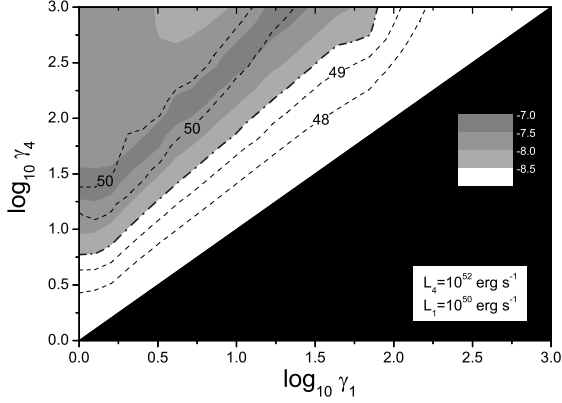


Fig. 5.— The peak flux at $T = T_{\text{exp}}$ of GeV γ -ray flares due to SSC emission for GRBs at the luminosity distance 10^{28}cm in the (γ_1, γ_4) parameter space. The regions where the GeV flux exceeds the *Fermi* LAT sensitivity (dash-dotted line) are shown by shaded contours, while the SSC emission calculated in the unshaded region could be not detected by the LAT. The model parameters here are the same as those adopted in the left panel of Figure 2. To compare with the associated X-ray component, the X-ray luminosities are also shown by the dashed contours and labeled by $\log_{10}[(\nu L_\nu)_X/\text{erg s}^{-1}]$.

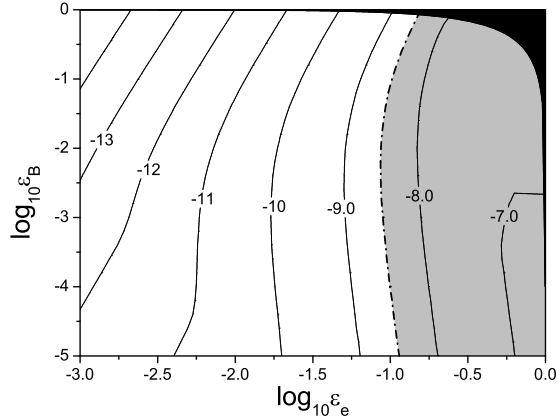


Fig. 6.— Variation of the peak flux at $T = T_{\text{exp}}$ of GeV γ -ray flares due to SSC emission for GRBs at the luminosity distance 10^{28}cm in the (ϵ_e, ϵ_B) parameter space. The contours are labeled by the values of $\log_{10}[(\nu F_\nu)_{\text{GeV}}/\text{erg s}^{-1}\text{cm}^{-2}]$. The region where the GeV flux exceeds the *Fermi* LAT sensitivity (dash-dotted line) is shaded. The black region is forbidden due to $\epsilon_B + \epsilon_e > 1$. The other model parameters are taken to be $L_1 = 10^{50}\text{ erg s}^{-1}$, $L_4 = 10^{52}\text{ erg s}^{-1}$, $\gamma_1 = 10$, $\gamma_4 = 300$, $p = 2.5$, $\Delta t_{\text{ej}} = 100\text{s}$ and $t_{\text{ej},\Lambda} = 400\text{s}$.

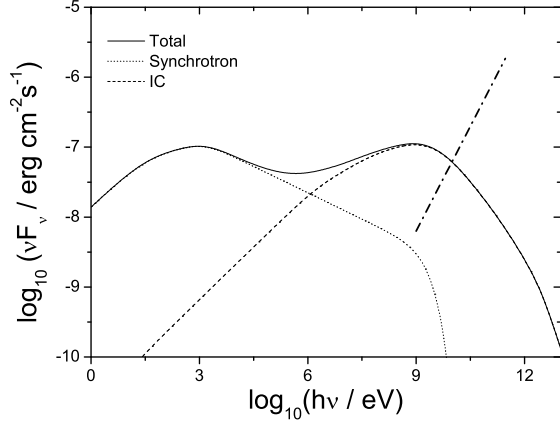


Fig. 7.— An example numerically-calculated spectrum by combining the synchrotron and SSC spectra contributed by the two shocks for the luminosity distance of 10^{28} cm. The dash-dotted line denotes the *Fermi* LAT sensitivity. The model parameters are taken to be $\epsilon_B = 0.03$, $\epsilon_e = 0.3$, $L_1 = 10^{50}$ erg s $^{-1}$, $L_4 = 10^{52}$ erg s $^{-1}$, $\gamma_1 = 10$, $\gamma_4 = 300$, $p = 2.5$, $\Delta t_{\text{ej}} = 100$ s and $t_{\text{ej,A}} = 400$ s.